

Article

# Fungus-Based MnO/Porous Carbon Nanohybrid as Efficient Laccase Mimic for Oxygen Reduction Catalysis and Hydroquinone Detection

Haoran Ge and Hailong Zhang \* 

School of Electrical and Automation Engineering, Nanjing Normal University, Nanjing 210023, China;  
haoran@163.com

\* Correspondence: 61204@njnu.edu.cn

**Abstract:** Developing efficient laccase-mimicking nanozymes via a facile and sustainable strategy is intriguing in environmental sensing and fuel cells. In our work, a MnO/porous carbon (MnO/PC) nanohybrid based on fungus was synthesized via a facile carbonization route. The nanohybrid was found to possess excellent laccase-mimicking activity using 2,2'-azinobis (3-ethylbenzthiazoline-6-sulfonic acid) diammmonium salt (ABTS) as the substrate. Compared with the natural laccase and reported nanozymes, the MnO/PC nanozyme had much lower  $K_m$  value. Furthermore, the electrochemical results show that the MnO/PC nanozyme had high electrocatalytic activity toward the oxygen reduction reaction (ORR) when it was modified on the electrode. The hybrid nanozyme could catalyze the four-electron ORR, similar to natural laccase. Moreover, hydroquinone (HQ) induced the reduction of oxABTS and caused the green color to fade, which provided colorimetric detection of HQ. A desirable linear relationship (0–50  $\mu$ M) and detection limit (0.5  $\mu$ M) were obtained. Our work opens a simple and sustainable avenue to develop a carbon–metal hybrid nanozyme in environment and energy applications.



**Citation:** Ge, H.; Zhang, H. Fungus-Based MnO/Porous Carbon Nanohybrid as Efficient Laccase Mimic for Oxygen Reduction Catalysis and Hydroquinone Detection. *Nanomaterials* **2022**, *12*, 1596. <https://doi.org/10.3390/nano12091596>

Academic Editor: Young-Seok Shon

Received: 3 April 2022

Accepted: 1 May 2022

Published: 8 May 2022

**Publisher's Note:** MDPI stays neutral with regard to jurisdictional claims in published maps and institutional affiliations.



**Copyright:** © 2022 by the authors. Licensee MDPI, Basel, Switzerland. This article is an open access article distributed under the terms and conditions of the Creative Commons Attribution (CC BY) license (<https://creativecommons.org/licenses/by/4.0/>).

**Keywords:** fungus; nanozyme; laccase; oxygen reduction reaction; hydroquinone detection

## 1. Introduction

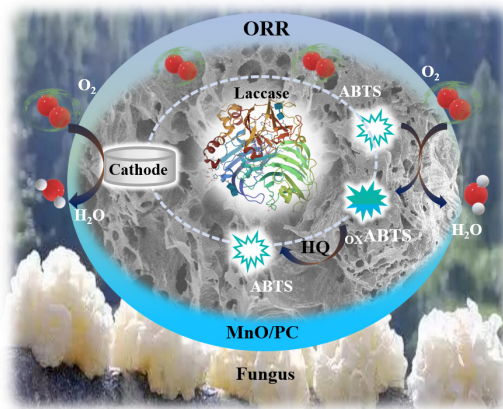
The oxygen reduction reaction (ORR) pathway is of great importance in meeting the specific needs of various ORR-related systems, such as biomimetic catalysis, fuel cells, and biosensing [1–5]. Using oxygen in aerobic metabolism under mild conditions is very attractive since  $O_2$  in the triplet ground state is very stable. Miraculously, metalloenzymes have provided an efficient and alternative solution to this obstacle under mild conditions [6–8]. As important metalloenzymes, laccases with copper as active sites catalyzed the oxidation of diverse biological and environmental substrates with oxygen [9–11]. In these reactions, laccase had the ability to catalyze the four-electron reduction of oxygen to water. Therefore, laccase has a wide application in the environmental and biosensing fields related to ORR [12–14]. More notably, laccase has attracted much attention in the research field of biofuel cells and bioelectrochemistry because it can realize the electrochemical catalytic reduction of oxygen molecules at low overpotential [15,16]. However, due to its fragile structure, the application of laccase in these fields is often limited by inherent defects, such as high cost, short active life, poor environmental tolerance, etc.

As new and robust artificial enzymes, nanozymes with highly specialized biological functions have wide practical applications, ranging from cancer therapy to biosensing, because of their advantages of catalytic activity and stability, cheap costs, and special physical–chemical properties [17–19]. The enzyme-like activity of nanozymes is flexibly related to its composition, structure, and size. Until now, some copper-based nanozymes have been reported to exhibit laccase-mimicking activity [20–22], but most nanozymes, such as gold nanoparticles, iron oxide nanoparticles, and carbon-based nanozymes, lack

laccase-mimicking activity [23,24]. Therefore, developing laccase-mimicking nanozymes that are low-cost and have a simple operation process, good biocompatibility, high activity, and stability is intriguing to pursue but remains challenging.

Due to its stable physical-chemical properties and three-dimensional interconnected porous structure, porous carbon material provides effective channels for material transmission, liquid flow, and gas diffusion, making it an important functional material used in adsorption, separation, sensing, energy storage, and catalysis [25–27]. Considering environmental and sustainable development problems, it is both a huge challenge and encouraging to use biomass-based carbon materials as the primary materials for chemical and enzymatic conversion processes [28,29]. Because widely distributed fungi mainly consist of polysaccharides, protein, and amino acids, they have both high-content carbon and heteroatom elements, such as oxygen, nitrogen, and sulfur. Therefore, they are economical, environmentally friendly, and sustainable carbon precursors for preparing heteroatoms-enriched carbon materials with the ability to complex with metal ions.

Recently, the enzyme-mimicking activity of manganese oxides ( $\text{MnO}_x$ ) has received considerable interest due to their attractive properties of being rich, cheap, a green alternative, and active, but the laccase-mimicking activity of manganese oxides remains scarce [30–32]. Our work used a biological fungus with a rich source and low price as raw material to prepare the  $\text{MnO}/\text{PC}$  hybrid (Scheme 1). The nanohybrid exhibited superior laccase-mimicking activity and high electrocatalytic activity for ORR. The combination of the respective properties of the two components achieved the enhanced catalytic performances of the hybrid nanzyme cooperatively. To the best of our knowledge, this is the first report to address a fungus-based nanzyme with laccase-mimicking activity, which provides a facile and sustainable strategy for expanding a carbon–metal hybrid nanzyme in environment and energy applications.



**Scheme 1.** Fungus-based  $\text{MnO}/\text{PC}$  nanohybrid as laccase mimic for ORR and HQ detection.

## 2. Experimental Section

### 2.1. Chemicals

*Tremella* produced in Fujian province was purchased from a local supermarket (Yangzhou, China). Pt/C (20 wt%) and 2,2'-azino-bis (3-ethylbenzothiazoline-6-sulfonic acid) (ABTS) were purchased from Sigma. Other reagents and chemicals were reagent-grade and were acquired from Sinopharm Chemical Reagent Co., Ltd. (Shanghai, China). Deionized water was used throughout.

### 2.2. Instrumentation and Characterization

X-ray diffraction (XRD) analysis was performed with a Bruker AXS D8 ADVANCE X-ray diffractometer (Germany). Scanning electron microscopy (SEM) images and energy-dispersive X-ray (EDX) were conducted on a Zeiss Supra 55 (Germany). X-ray photoelectron spectroscopy (XPS) measurements were conducted on an ESCALAB-MKII 250 photoelec-

tron spectrometer (UK), using Al/K $\alpha$  as the X-ray source for excitation. UV-vis spectra were recorded using a UV-2501 (Japan). The structure was analyzed by Raman spectroscopy (DXR, GX-PT-2412, Thermo, USA) with a 532 nm laser as the excitation wavelength.

### 2.3. Synthesis of MnO/PC Nanohybrid

As shown in Scheme 2, the obtained tremella was first cleaned and soaked in deionized water for 2 h and was then heated for more than 30 min until it became sticky. A 0.5 M manganese acetate solution was mixed with the sticky tremella. The mixture was stirred for about half an hour at room temperature and left for 48 h. The mixed system was frozen at  $-90^{\circ}\text{C}$  for 48 h to be dehydrated with a freeze-dryer. Next, the as-prepared sample was carbonized at  $800^{\circ}\text{C}$  for 2 h with a ramping rate of  $5^{\circ}\text{C min}^{-1}$  in the protection of  $\text{N}_2$ . The sample was then washed with ethanol and water and finally dried at  $60^{\circ}\text{C}$ . A MnO/PC-700 nanohybrid was synthesized under the same procedure, except that  $700^{\circ}\text{C}$  was used as the calcination temperature. The porous carbon was obtained via the same synthetic procedure, except for the absence of manganese ions.



**Scheme 2.** Schematic illustration of the synthesis of MnO/PC nanohybrid based on the tremella.

### 2.4. Laccase-Mimicking Activity of MnO/PC Nanohybrid

The laccase-mimicking activity of the MnO/PC nanohybrid was measured using catalytic oxidation of the typical laccase substrate ABTS at  $20^{\circ}\text{C}$ . For a typical oxidation experiment, 50  $\mu\text{L}$  MnO/PC dispersion (5 mg/mL) and 60  $\mu\text{L}$  20 mM ABTS were introduced in 2.890 mL of 0.2 M HAc-NaAc at pH 4.0. The UV-vis spectra of the system were recorded after 20 min.

### 2.5. ORR Electrocatalytic Activity of MnO/PC Nanohybrid

Electrochemical measurements were recorded on an electrochemical workstation (VMP3, Biologic, Seyssinet-Pariset, France) with a conventional three-electrode system. The electrode system was composed of a Pt wire as the counter electrode, Ag/AgCl as the reference electrode, and a rotating ring-disk electrode (RRDE) as the working electrode. The detailed electrochemical procedures are shown in the Supporting Information.

### 2.6. Determination of Hydroquinone

For a typical determination experiment, 50  $\mu\text{L}$  MnO/PC dispersion (5 mg/mL) and 60  $\mu\text{L}$  of 10 mM ABTS were introduced in 0.2 M HAc-NaAc at pH 4.0. After reaction for 10 min, ABTS turned into green oxABTS. Next, HQ of different concentrations was added, and the green color faded. Two minutes later, the concentration of HQ was obtained according to the absorbance at 416 nm. The lake real sample was filtered and introduced in 0.2 M HAc-NaAc at pH 4.0, and the same procedure was used to analyze the HQ concentration in the system.

## 3. Results and Discussion

### 3.1. Characterizations of MnO/PC Nanohybrid

As a typical fungus, tremella consisting mainly of polysaccharides was selected as the precursor and template for obtaining the carbon-loaded metal nanohybrid with high-temperature pyrolysis. Scheme 2 summarizes the synthesis strategy of the formation of the hybrid. Tremella rich in oxygen-containing functional groups contributes to the specific

affinity with Mn(II) ion and the formation of carbon loaded with the MnO hybrid after the calcination.

The microstructure of the MnO/PC nanohybrid, based on the fungus's carbon obtained at 800 °C, was first characterized by scanning electron microscopy (SEM). As seen in Figure 1A,B, the MnO/PC nanohybrid exhibited macropores, and shell-like structured MnO crystals were loaded on the carbon surface. The SEM image with high magnification shows that the shell-like structured MnO was composed of many nanoparticles with small sizes. For the individual biomass carbon obtained in the absence of metal ion (Figure S1), only the porous carbon was observed, and the surface of the carbon was approximately smooth. The EDX result demonstrated that the nanohybrid was composed of Mn, C, and O elements (Figure 1C). Different from many earlier porous carbon nanomaterials based on biomass cellulose, the process of KOH activation was avoided when tremella was used as the biomass.

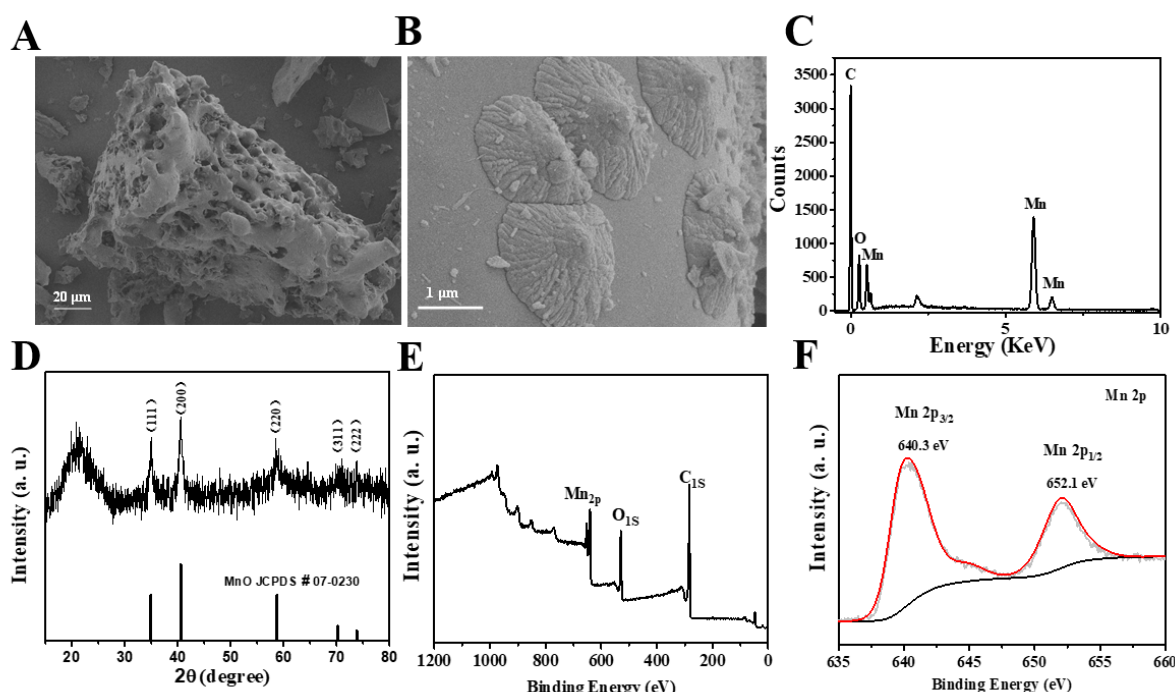


**Figure 1.** (A,B) SEM images of MnO/PC nanohybrid with different magnifications. EDX spectroscopy (C), XRD patterns (D), XPS survey scan (E), and high-resolution Mn 2p XPS spectrum (F) of MnO/PC nanohybrid.

The wide-angle X-ray diffraction (XRD) pattern of the hybrid is shown in Figure 1D. The broad peak between 20 to 30° indicates the amorphous carbon. Five diffraction peaks at 34.91, 40.55, 58.72, 70.17, and 73.70° indexed to (111), (200), (220), (311), and (222) crystal planes of MnO (JCPDS no. 07-0230) indicate that MnO was formed in the system. In addition, since the relative intensity of the MnO peaks was weak, the shell-like structured MnO in the nanohybrid may have poor crystallinity. Because no other diffraction peaks were obtained, pure MnO was present. Raman spectroscopy was also used to characterize the structure of the nanohybrid (Figure S2). As seen, the characteristic peak at  $646.8\text{ cm}^{-1}$  was attributed to the Mn–O vibration [33]. Since the two typical peaks centering at  $1348.5\text{ cm}^{-1}$  (D-band) and  $1590.6\text{ cm}^{-1}$  (G-band) with the relative intensity ratio of the D-band to the G-band ( $I_D/I_G$ ) was 0.88, the graphitic carbon phase was present in the nanohybrid [34].

XPS spectra were used to demonstrate the surface composition and chemical valence state of the MnO/PC nanohybrid. The full-scan spectrum demonstrated that the hybrid was also mainly composed of the elements Mn, O, and C (Figure 1E), suggesting the

formation of a manganese oxide and carbon hybrid. The surficial atomic concentration of the Mn, C, and O elements of the hybrid was about 6.79%, 76.16%, and 17.05%, respectively. According to the high-resolution Mn 2p XPS spectrum of the hybrid (Figure 1F), the peaks at 640.3 and 652.1 eV were caused by Mn 2p<sub>1/2</sub> and Mn 2p<sub>3/2</sub>, respectively, suggesting the formation of MnO. Furthermore, an energy separation of 11.8 eV also demonstrated Mn 2p<sub>3/2</sub> and Mn 2p<sub>1/2</sub> in MnO [35,36]. The presence of MnO was further confirmed by the O 1s spectrum. As seen in Figure S3, three typical peaks at 530.1, 531.6, and 532.9 eV are caused by Mn-O-Mn, Mn-O-H, and H-O-H, respectively.

### 3.2. Laccase-Mimicking Activity of MnO/PC Nanohybrid

After characterizing its structure, the laccase-mimicking activity of the MnO/PC nanohybrid using the typical ABTS as the substrate was measured. Figure 2A shows that the MnO/PC nanohybrid could catalyze the oxidation of ABTS to form the typical green color rapidly. On the contrary, the individual ABTS system was nearly colorless. There was a significantly strong absorbance at 416 nm of the system with the hybrid nanozyme, indicating that the MnO/PC nanohybrid had superior laccase-mimicking activity. By comparison, the laccase-mimicking activity of PC and Mn<sup>2+</sup> was studied and we found that PC could only weakly catalyze ABTS oxidation and that Mn<sup>2+</sup> had no catalytic activity for ABTS oxidation under the same experimental conditions.

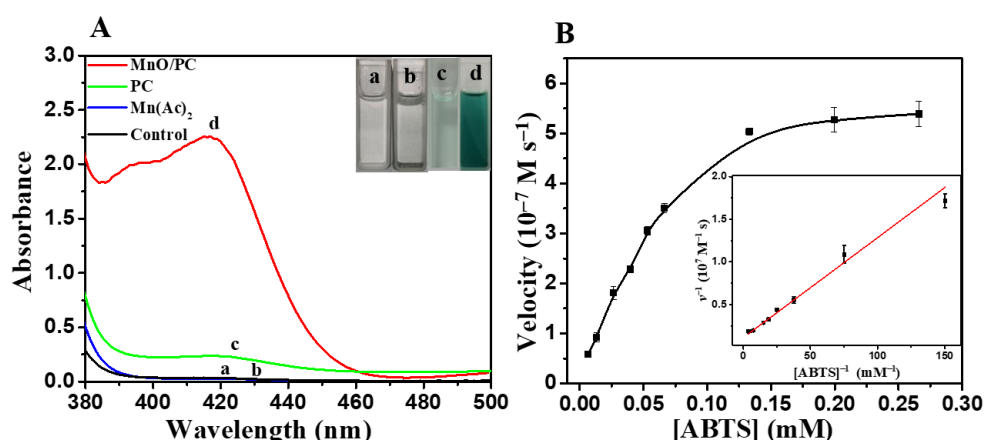


**Figure 2.** (A) Typical UV-vis spectra of different systems: (a) ABTS + buffer, (b) ABTS + Mn(Ac)<sub>2</sub> + buffer, (c) ABTS + PC + buffer, and (d) ABTS + MnO/PC nanohybrid + buffer. (B) Steady-state kinetic assay and kinetic analysis by double reciprocal plots (inset) of the MnO/PC nanohybrid with ABTS as the substrate.

To confirm the role of the MnO/PC nanohybrid obtained at 800 °C in determining laccase-like activity, the catalytic activity of the MnO/PC-700 nanohybrid was further studied. Figure S4 shows that the porous structure of carbon and the structure of MnO changed greatly at the calcination temperature of 700 °C. As shown in Figure S5, the MnO/PC-700 nanohybrid can also catalyze the oxidation of ABTS to produce green color, displaying absorption at 416 nm. Because the laccase-like activity of MnO/PC-800 was higher than that of MnO/PC-700, the cooperative effect of the porous-structured carbon and shell-like structured MnO was favorable for the substrates to bind and activate. Notably, the laccase-mimicking activity of the hybrid remained almost unchanged after more than one year, indicating the high stability of the hybrid nanozyme.

Similar to laccase, the enzyme-like activity of MnO/PC nanohybrid depended on the pH and temperature. As seen in Figure S6A, the laccase-mimicking activity of the nanozyme decreased with the pH but still exhibited more than 90% activity at pH 5.0. As seen in Figure S6B, the laccase-mimicking activity of MnO/PC nanohybrid increased with the increase of temperature. Because the laccase-mimicking activity of the hybrid did not

change much in the temperature range of 20–35 °C, it was free to use the hybrid nanozyme at room temperature.

The kinetic parameters were obtained to investigate the laccase-mimicking activity of the MnO/PC nanohybrid. The typical Michaelis–Menten curves were obtained within certain concentration ranges of ABTS (Figure 2B), and then  $K_m$  and  $V_{max}$  were obtained according to the Lineweaver–Burk linear fitting equation (Table 1). As seen, the MnO/PC nanohybrid had a much lower  $K_m$  and higher  $V_{max}$  [37–40]. Since pure PC exhibited poor laccase-like activity, the presence of MnO provided active sites for the laccase-mimicking activity of the MnO/PC nanohybrid. Recently, the enzyme-like activity of manganese oxides (MnOx) has received considerable attraction due to its outstanding catalytic performance. Wang, et al., reported the laccase-like activity of manganese oxides such as MnO<sub>2</sub> and Mn<sub>3</sub>O<sub>4</sub> using ABTS as the substrate [40], but the laccase-like activity of MnO has never been reported. As seen in Table 1, the  $K_m$  and  $V_{max}$  for the laccase-like activity of the MnO/PC nanohybrid with ABTS as the substrate was much better than that of the reported manganese oxides. Thus, the synergistic effects of MnO and PC contributed to the superior catalytic activity of the MnO/PC hybrid. For the MnO/PC nanohybrid with the integration of PC and MnO, the porous structure in the catalysts provided a path for the reactant and product molecules to diffuse in and out freely and resulted in high affinity towards substrates [41–43]. Furthermore, the shell-like MnO distributed on the porous carbon surface was composed of numerous nanoparticles with small sizes. The dispersed hierarchical structure enabled plentiful active sites provided by small-sized MnO nanoparticles, accessible to the substrates during the reaction [44,45]. These factors all led to the high laccase-like activity of the hybrid nanozyme. Notably, the  $K_m$  for the laccase-like activity of the MnO/PC nanohybrid with ABTS as the substrate was similar to the  $K_m$  for the 3DGF/Pt NC nanohybrid. This further confirmed that the porous structure of carbon greatly contributed to the high affinity of the substrate toward the nanozymes [39]. Evidently, the fungus-based MnO/PC hybrid nanozyme had the advantages of being low cost, requiring a simple operation process, and being renewable. In addition to a laccase-mimicking nanozyme, the use of immobilized natural laccase is also important in practice. For comparison, the kinetic parameters of the immobilized laccase with ABTS as the substrate were provided. Table 1 shows that the MnO/PC nanohybrid had relatively higher affinity and catalytic activity than that of the immobilized natural laccase. Thus, as a kind of laccase-like mimic with high catalytic activity, the MnO/PC nanohybrid has potential application in practice.

**Table 1.** Comparison of the apparent Michaelis–Menten constant ( $K_m$ ) and maximum reaction rate ( $V_{max}$ ) for different catalysts using ABTS as the substrate.

Catalyst	$K_m$ (mM)	$V_{max}$ ( $10^{-7}$ M s <sup>-1</sup> )	Reference
Silica gel-laccase	0.417	3.317	[37]
Mesoporous carbon-laccase	0.550	3.125	[38]
3D GF/Pt NC	0.172	24.6	[39]
$\alpha$ -MnO <sub>2</sub>	1.97	1.68	[40]
$\beta$ -MnO <sub>2</sub>	4.54	1.34	[40]
Mn <sub>3</sub> O <sub>4</sub>	2.22	2.19	[40]
MnO/PC nanohybrid	0.10	8.94	This study

### 3.3. ORR Electrocatalytic Activity of MnO/PC Nanohybrid

Motivated by the superior laccase-like activity of the MnO/PC nanohybrid, the ORR electrocatalytic activity of the obtained laccase-mimicking MnO/PC nanohybrid was further studied with the electrochemical method. The ORR electrocatalytic activities of the MnO/PC nanohybrid were evaluated in O<sub>2</sub>-saturated 0.1 M KOH using a rotating ring-disk electrode (RRDE). The CV profiles for the MnO/PC nanohybrid in N<sub>2</sub> and O<sub>2</sub> saturated 0.1 M KOH are given in Figure 3A. An obvious peak was observed in the O<sub>2</sub>-saturated

0.1 M KOH solution, but no peak was obtained in the  $\text{N}_2$ -saturated KOH solution. Thus, the MnO/PC nanohybrid exhibited ORR electrocatalytic activity.

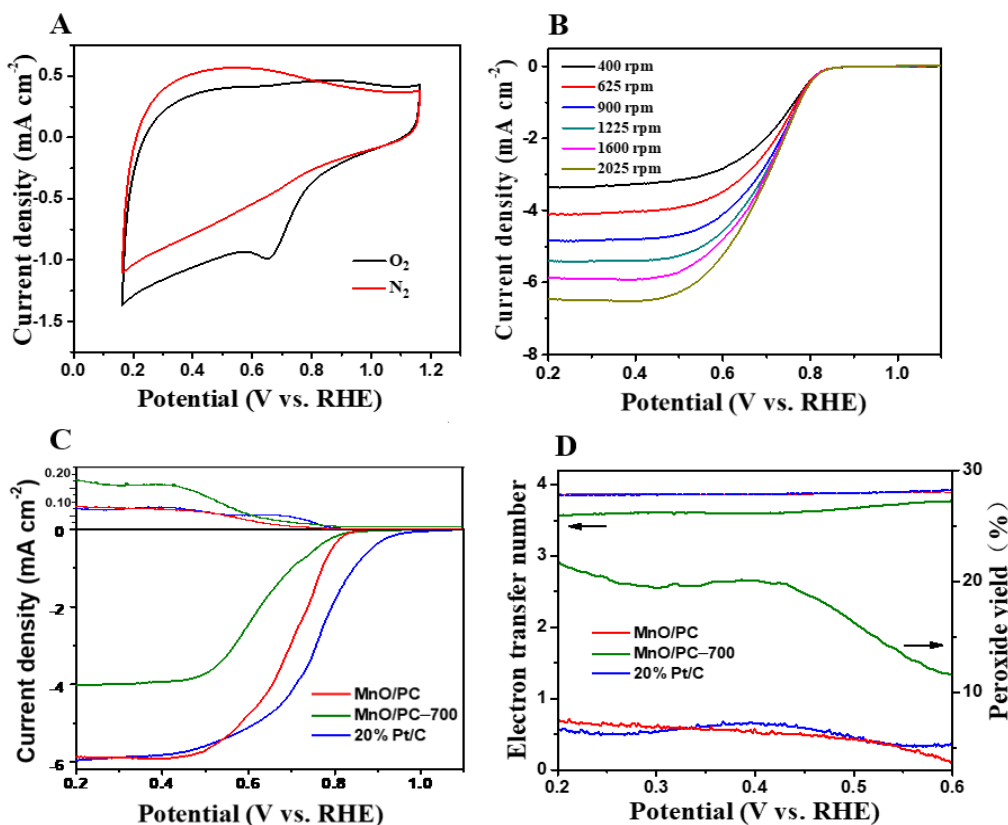


**Figure 3.** (A) CV curves of MnO/PC nanohybrid at 20 mV s<sup>-1</sup> in  $\text{N}_2$  and  $\text{O}_2$ -saturated 0.1 M KOH. (B) LSV curves of MnO/PC nanohybrid at different electrode rotation rates in  $\text{O}_2$ -saturated 0.1 M KOH. Inset shows K-L plots of ORR. (C) RRDE voltammograms of the MnO/PC nanohybrid, MnO/PC-700 nanohybrid, and 20% Pt/C in  $\text{O}_2$ -saturated 0.1 M KOH at 1600 rpm. (D) The transferred electron number (*n*) and  $\text{HO}_2^- \text{H}_2\text{O}_2$  yield derived from the RRDE measurements in (C).

The linear sweep voltammetry (LSV) curves of the porous carbon and MnO/PC nanohybrid are shown in Figure S7. As seen, the MnO/PC nanohybrid showed notably enhanced performances, i.e., increased limiting currents and half-wave potentials. Compared with individual porous carbon, the superior ORR activity of the MnO/PC nanohybrid may be ascribed to the facile mass transport of the reactants and electrons caused by the porous structure and synergistic effect between MnO and PC. Figure 3B presents the LSV curves of the MnO/PC nanohybrid with various rotating rates from 400 to 2025 rpm and the corresponding K-L plots of different potentials. It can be seen from a set of LSV curves of MnO/PC that the current density increased when the rotating speed increased (Figure 3B). The current density achieved the diffusion, limiting current well at different rotation speed. The Koutecky-Levich (K-L) plots under different potentials displayed excellent linearity, and there was almost no difference between these plots, suggesting first-order reaction kinetics with respect to the dissolved oxygen in electrolyte and similar electron transfer number *n* at different potentials of the hybrid nanozyme. The transferred electron number *n* for the MnO/PC hybrid nanozyme was analyzed to be ca. 4 at the potential range from 0.20 to 0.50 V, demonstrating that the ORR process of the MnO/PC nanohybrid followed a typical four-electron pathway.

The LSV curves of the MnO/PC nanohybrid, MnO/PC-700 nanohybrid, and 20 wt% Pt/C are shown in Figure 3C. The half-wave potential for the MnO/PC hybrid was about 0.73 V, with the limiting currents of  $-5.87 \text{ mA cm}^{-2}$ . The half-wave potential difference for

the hybrid and 20 wt% Pt/C was only about 60 mV, and the limited current of MnO/PC nanohybrid was almost close to that of 20 wt% Pt/C. Compared with the MnO/PC nanohybrid, the MnO/PC-700 nanohybrid displayed a more negative half-wave potential and a lower limiting current density, which further revealed that the cooperative effect of MnO and PC in the nanohybrid was helpful to improve the ORR catalytic performance significantly. A comparison of the ORR electrochemical performances for the MnO/PC nanohybrid with the relevant catalysts and Pt/C is provided in Table S1. As seen, the ORR electrochemical performances of the MnO/PC nanohybrid was much better than that of the reported pure MnO catalyst. Compared with the most reported MnO/C hybrid, the MnO/PC nanohybrid exhibited an efficient four-electron pathway and high limiting current density, close to the commercial Pt/C-20%.

According to the ring and disk current of the MnO/PC nanohybrid, MnO/PC-700 nanohybrid, and 20 wt% Pt/C (Figure 3C), the transferred electron number ( $n$ ) and percentage yield of  $\text{HO}_2^-$  are shown in Figure 3D. The electron number higher than 3.88 in the scanning potential range of 0.2–0.6 V was coincidental with the K–L plot results, further indicating a four-electron electrochemistry reaction process. Simultaneously, the percentage yield of  $\text{HO}_2^-$  for the MnO/PC nanohybrid in alkaline environments was lower than 7.5%, which was close to that of the 20 wt% Pt/C. The MnO/PC-700 exhibited a lower  $n$  (3.62) and higher  $\text{HO}_2^-$  yields (12.5–22.0%) in the scanning potential range of 0.2–0.6 V, demonstrating that the MnO/PC nanohybrid can provide a high ORR activity and an efficient four-electron pathway. This further confirmed that the structure of a MnO/PC nanohybrid matters greatly in determining the superior catalytic activity. As seen in Figure S8, the nanohybrid in the ORR electrochemical activity is durable. Because the MnO/PC nanohybrid catalyzed the four-electron ORR efficiently, similar to natural laccase, the nanozyme has potential as a cathode catalyst for fuel cells.

### 3.4. Sensing HQ Based on MnO/PC Nanohybrid

Since hydroquinone (HQ) has been recognized as one of the biggest environmental pollutants, it is important to fabricate a facile and sensitive method to detect HQ. Although nanozymes have been widely applied in sensing environmental pollutants with the colorimetric method, the laccase-mimicking nanozyme is seldom used to detect phenols. Due to the superior laccase-like activity of the MnO/PC nanohybrid, it is expected to fabricate HQ colorimetric sensors through regulating the catalytic activity of the nanohybrid.

The MnO/PC nanohybrid catalyzed the oxidation of ABTS into green-colored oxABTS effectively at room temperature, but the addition of HQ into the system led to a fading blue color, with a decrease in the absorbance at about 416 nm (Figure 4A). With the increase in HQ concentration, the decrease in the absorbance was enhanced. Based on this, the colorimetric detection for HQ concentration was developed using the absorbance decrease of ABTS. Figure 4B shows the calibration curve for HQ, and the absorbance at 416 nm decreased linearly with the increasing concentration of HQ in the range of 0 to 50  $\mu\text{M}$ , with a detection limit of 0.2  $\mu\text{M}$  ( $S/N = 3$ ).

As seen in Table 2, HQ colorimetric sensors have been developed using different nanozymes. Although a HQ colorimetric sensor based on the peroxidase-like and oxidase-like activity of a nanozyme with 3,3',5,5'-tetramethylbenzidine (TMB) as the substrate has been widely reported in some earlier studies, studies on the HQ colorimetric sensor based on laccase-like nanozymes with ABTS as the substrate are scarce. Compared with the earlier studies, the proposed colorimetric sensor exhibited a desirable LOD and linear range. Furthermore, since the hybrid nanozyme was synthesized via a facile and sustainable route, the colorimetric laccase mimetic strategy has potential applications in environmental fields.

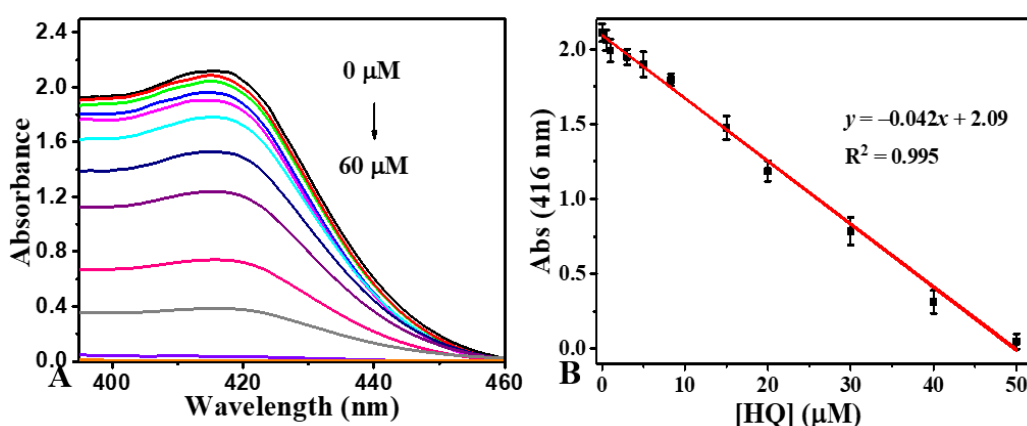
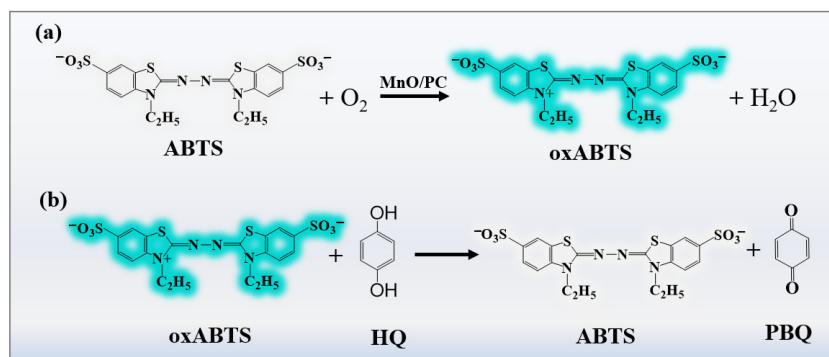


**Figure 4.** (A) The absorbance spectra of the MnO/PC-ABTS system in the presence of different concentrations of HQ (0–60  $\mu$ M). (B) The linearity of the detection against the concentration of HQ, ranging from 0 to 50  $\mu$ M.

**Table 2.** Comparison of the colorimetric method using the MnO/PC hybrid nanozyme with other reported nanozymes for HQ determination.

Probes	Linear Range ( $\mu$ M)	LOD ( $\mu$ M)	Reference
Cu-CAP	0–100	0.023	[46]
Pt/CdS nanocomposite	1–10	0.165	[47]
ZnFe <sub>2</sub> O <sub>4</sub> /ZnO	0–150	3.75	[48]
NiMnO <sub>3</sub> composites	1–85	0.68	[49]
NiCo <sub>2</sub> O <sub>4</sub> microspheres	5–110	2.7	[50]
3D GF/Pt nanohybrid	0.05–1, 1–50	0.01	[39]
MnO/PC nanohybrid	0–50	0.5	This study

The mechanism of sensing HQ using the chromogenic substrate ABTS and the MnO/PC nanohybrid-catalyzed ABTS color reaction is shown in Scheme 3. First, the color of the ABTS changed into green-colored oxABTS due to the superior laccase-like activity of the MnO/PC nanohybrid, which was accompanied by a sharp increased absorbance at 416 nm (Scheme 3a). Second, due to the strong reducibility of HQ, the redox reaction occurred between HQ and oxABTS after the addition of the HQ. Green-colored oxABTS changed back into colorless ABTS, which was accompanied by a decrease in the absorbance at 416 nm. At the same time, HQ was oxidized to the p-benzoquinone tautomer (PBQ) (Scheme 3b).



**Scheme 3.** The schematic mechanism of colorimetric detection of HQ based on the MnO/PC nanohybrid. (a) ABTS changed into green-colored oxABTS due to the superior laccase-like activity of the MnO/PC nanohybrid, (b) Green-colored oxABTS changed back into colorless ABTS due to the redox reaction.

To investigate the selectivity of the method, other substances, including cations, anions, and some phenols, were introduced into the system using the same experimental procedure. Compared with the signal of 30  $\mu\text{M}$  HQ, the decrease in absorbance at 416 nm after the addition of most substances was not observed, demonstrating desirable selectivity for HQ detection (Figure S9). Similar to many earlier studies, catechol significantly interfered with hydroquinone detection [51–53]. The results indicate the developed method can analyze total hydroquinone and catechol in the presence of catechol. The practical application of the HQ sensor based on the MnO/PC nanohybrid was also demonstrated by adding a standard recovery experiment in the real sample. Table S2 shows that the recovery of the tested samples ranged from 96.0 to 106.3% and the RSDs were all below 4.6%. Thus, it is reliable to use the MnO/PC-based HQ sensor to detect HQ in practical applications.

#### 4. Conclusions

Herein, an effective strategy for designing fungus-based laccase-mimicking nanozyme was proposed. A shell-like structured, MnO-loaded, porous carbon nanohybrid was synthesized through a simple calcination method. The MnO/PC hybrid catalyzed the oxidation of the laccase substrate ABTS and possessed excellent intrinsic laccase-like activities. Furthermore, the hybrid nanozyme played a crucial role in the ORR electrocatalytic activity with half-wave potentials of 0.73 V vs. RHE in 0.1 M KOH, limiting current density of  $-5.87 \text{ mA cm}^{-2}$  and the electron transfer number to 4. Moreover, the colorimetric HQ sensor due to the oxidase-like activity of the hybrid nanozyme was developed, with the well linear relationship ranging from 0 to 50  $\mu\text{M}$  and a detection limit of 0.5  $\mu\text{M}$ . Our work provides a new and sustainable approach for the development of high-performance carbon–metal hybrid nanozymes.

**Supplementary Materials:** The following supporting information can be downloaded at <https://www.mdpi.com/article/10.3390/nano12091596/s1>, Figure S1: (A,B) SEM images of porous carbon with different magnifications; Figure S2: Raman spectra of MnO/PC nanohybrid; Figure S3: High-resolution O1s XPS spectra of MnO/PC nanohybrid; Figure S4: SEM images of MnO/PC nanohybrid obtained at 700 °C with different magnifications; Figure S5: Typical UV-vis spectra of the oxidation of ABTS by MnO/PC nanohybrid obtained at 700 and 800 °C; Figure S6: The influence of pH (A) and temperature (B) on the relative activity of the MnO/PC nanohybrid; Figure S7: LSV curves of PC and MnO/PC nanohybrid at 1600 rpm in O<sub>2</sub>-saturated 0.1 M KOH; Figure S8: (A) Chronoamperometric curves of MnO/PC nanohybrid and Pt/C in O<sub>2</sub>-saturated 0.1 M KOH with a constant potential 0.65 V (vs. RHE). (B) Chronoamperometric curves of MnO/PC nanohybrid by adding of 3 M methanol after 330 s in O<sub>2</sub>-saturated 0.1 M KOH with a constant potential 0.65 V (vs. RHE); Figure S9: Effect of different phenols and ions on HQ sensing with adding equal amounts of phenols and 10-fold other compounds; Table S1. Comparison of the ORR electrochemical performances of MnO/PC nanohybrid with the reported catalysts and Pt/C; Table S2: Determination of HQ in real sample using our colorimetical method. References [54–61] are cited in the Supplementary Materials.

**Author Contributions:** Conceived and designed the experiments and wrote the manuscript, H.G. and H.Z.; conducted the experiments, H.G. All authors have read and agreed to the published version of the manuscript.

**Funding:** This research received no external funding.

**Institutional Review Board Statement:** Ethical review and approval were waived for this study because no experiment involved humans or animals.

**Informed Consent Statement:** Not applicable.

**Data Availability Statement:** Data are available upon reasonable request to the authors.

**Conflicts of Interest:** The authors declare no conflict of interest.

## References

- Wu, Y.; Chen, Y.; Wang, H.; Wang, C.; Wang, A.; Shuai, Z.; Li, X.; Sun, D.; Jiang, J. Efficient ORR Electrocatalytic Activity of Peanut Shell-Based Graphitic Carbon Microstructures. *J. Mater. Chem. A* **2018**, *6*, 12018–12028. [[CrossRef](#)]
- Nadeem, M.; Yasin, G.; Arif, M.; Bhatti, M.H.; Sayin, K.; Mehmood, M.; Yunus, U.; Mehboob, S.; Ahmed, I.A. Pt-Ni@PC900 Hybrid Derived from Layered-Structure Cd-MOF for Fuel Cell ORR Activity. *ACS Omega* **2020**, *5*, 2123–2132. [[CrossRef](#)]
- Khan, I.; Qian, Y.; Badshah, A.; Nadeem, M.; Zhao, D. Highly Porous Carbon Derived from MOF-5 as a Support of ORR Electrocatalysts for Fuel Cells. *ACS Appl. Mater. Interfaces* **2016**, *8*, 17268–17275. [[CrossRef](#)] [[PubMed](#)]
- Khan, A.; Gunawan, C.; Zhao, C. Oxygen Reduction Reaction in Ionic Liquids: Fundamentals and Applications in Energy and Sensors. *ACS Sustain. Chem. Eng.* **2017**, *5*, 3698–3715. [[CrossRef](#)]
- Lv, H.; Liu, Z.; Chen, J.; Ikram, M.; Bai, X.; Wang, J.; Sun, B.; Kan, K.; Shi, K. Enhanced room-temperature NO<sub>2</sub> sensing properties of biomorphic hierarchical mixed phase WO<sub>3</sub>. *Nanoscale* **2020**, *12*, 24285–24295. [[CrossRef](#)]
- Lin, Y. Rational design of metalloenzymes: From single to multiple active sites. *Coord. Chem. Rev.* **2017**, *336*, 1–27. [[CrossRef](#)]
- Morokuma, K.; Musaev, D.; Vreven, T.; Basch, H.; Torrent, M.; Khoroshun, D. Model studies of the structures, reactivities, and reaction mechanisms of metalloenzymes. *IBM J. Res. Dev.* **2001**, *45*, 367–395. [[CrossRef](#)]
- Goralski, S.; Rose, M. Emerging artificial metalloenzymes for asymmetric hydrogenation reactions. *Curr. Opin. Chem. Biol.* **2021**, *66*, 102096. [[CrossRef](#)]
- Hilgers, R.; Kabel, M.; Vincken, J. Reactivity of p-Coumaroyl Groups in Lignin upon Laccase and Laccase/HBT Treatments. *ACS Sustain. Chem. Eng.* **2020**, *8*, 8723–8731. [[CrossRef](#)]
- Zhou, H.; Qiu, X.; Yang, D.; Xie, S. Laccase and Xylanase Incubation Enhanced the Sulfomethylation Reactivity of Alkali Lignin. *ACS Sustain. Chem. Eng.* **2016**, *4*, 1248–1254. [[CrossRef](#)]
- Flander, L.; Rouau, X.; Morel, M.-H.; Autio, K.; Seppänen-Laakso, T.; Kruus, K.; Buchert, J. Effects of Laccase and Xylanase on the Chemical and Rheological Properties of Oat and Wheat. *J. Agric. Food Chem.* **2008**, *56*, 5732–5742. [[CrossRef](#)] [[PubMed](#)]
- Dai, Y.; Yin, L.; Niu, J. Laccase-Carrying Electrospun Fibrous Membranes for Adsorption and Degradation of PAHs in Shoal Soils. *Environ. Sci. Technol.* **2011**, *45*, 10611–10618. [[CrossRef](#)] [[PubMed](#)]
- Lin, Y. Biodegradation of aromatic pollutants by metalloenzymes: A structural-functional-environmental perspective. *Coord. Chem. Rev.* **2021**, *434*, 213774. [[CrossRef](#)]
- Longe, F.; Couvreur, J.; Grandchamp, M.; Garnier, G.; Allais, F.; Saito, K. Importance of Mediators for Lignin Degradation by Fungal Laccase. *ACS Sustain. Chem. Eng.* **2018**, *6*, 10097–10107. [[CrossRef](#)]
- Adam, C.; Scodeller, P.; Grattieri, M.; Villalba, M.; Calvo, E.J. Revisiting direct electron transfer in nanostructured carbon laccase oxygen cathodes. *Bioelectrochemistry* **2016**, *109*, 101–107. [[CrossRef](#)] [[PubMed](#)]
- Patra, S.; Sene, S.; Mousty, C.; Chausse, A.; Legrand, L.; Steunou, N. Design of Laccase-Metal Organic Framework-Based Bioelectrodes for Biocatalytic Oxygen Reduction Reaction. *ACS Appl. Mater. Inter.* **2016**, *53*, 8505–8516. [[CrossRef](#)] [[PubMed](#)]
- Liu, L.; Hao, Y.; Deng, D.; Xia, N. Nanomaterials-Based Colorimetric Immunoassays. *Nanomaterials* **2019**, *9*, 316. [[CrossRef](#)] [[PubMed](#)]
- Wu, J.; Wang, X.; Wang, Q.; Lou, Z.; Li, S.; Zhu, Y.; Qin, L.; Wei, H. Nanomaterials with Enzyme-like Characteristics (nanozymes): Next-generation artificial enzymes (II). *Chem. Soc. Rev.* **2019**, *48*, 1004–1076. [[CrossRef](#)]
- Huang, Y.; Ren, J.; Qu, X. Nanozymes: Classification, Catalytic Mechanisms, Activity Regulation, and Applications. *Chem. Rev.* **2019**, *119*, 4357–4412. [[CrossRef](#)]
- Zhang, S.; Lin, F.; Yuan, Q.; Liu, J.; Li, Y.; Liang, H. Robust magnetic laccase-mimicking nanozyme for oxidizing o-phenylenediamine and removing phenolic pollutants. *J. Environ. Sci.* **2020**, *88*, 103–111. [[CrossRef](#)]
- Wang, J.; Huang, R.; Qi, W.; Su, R.; Binks, B.; He, Z. Construction of a bioinspired laccase-mimicking nanozyme for the degradation and detection of phenolic pollutants. *Appl. Catal. B* **2019**, *254*, 452–462. [[CrossRef](#)]
- Ren, X.; Liu, J.; Ren, J.; Tang, F.; Meng, X. One-pot synthesis of active copper containing carbon dots with laccase-like activities. *Nanoscale* **2015**, *7*, 19641–19646. [[CrossRef](#)] [[PubMed](#)]
- Jin, J.; Li, L.; Zhang, L.; Luan, Z.; Xin, S.; Song, K. Progress in the Application of Carbon Dots-Based Nanozymes. *Front. Chem.* **2021**, *9*, 748044. [[CrossRef](#)]
- Lin, Y.; Ren, J.; Qu, X. Nano-Gold as Artificial Enzymes: Hidden Talents. *Adv. Mater.* **2014**, *26*, 4200–4217. [[CrossRef](#)] [[PubMed](#)]
- Chen, Y.; Jiao, L.; Yan, H.; Xu, W.; Wu, Y.; Wang, H.; Gu, W.; Zhu, C. Hierarchically Porous S/N Codoped Carbon Nanozymes with Enhanced Peroxidase-like Activity for Total Antioxidant Capacity Biosensing. *Anal. Chem.* **2020**, *92*, 13518–13524. [[CrossRef](#)] [[PubMed](#)]
- Tian, Y.; Ren, Q.; Chen, X.; Li, L.; Lan, X. Yeast-Based Porous Carbon with Superior Electrochemical Properties. *ACS Omega* **2022**, *7*, 654–660. [[CrossRef](#)]
- Barton, S.; Evans, M.; Halliop, B.; MacDonald, J. Anodic Oxidation of Porous Carbon. *Langmuir* **1997**, *13*, 1332–1336. [[CrossRef](#)]
- Hoang, V.; Dirhab, K.; Gome, V. Iodine doped composite with biomass carbon dots and reduced graphene oxide: A versatile bifunctional electrode for energy storage and oxygen reduction reaction. *J. Mater. Chem. A* **2019**, *7*, 22650–22662. [[CrossRef](#)]
- Li, Y.; Li, C.; Qi, H.; Yu, K.; Li, X. Formation mechanism and characterization of porous biomass carbon for excellent performance lithium-ion batteries. *RSC Adv.* **2018**, *8*, 12666–12671. [[CrossRef](#)]

30. Tang, W.; Fan, W.; Zhang, W.; Yang, Z.; Li, L.; Wang, Z.; Chiang, Y.; Liu, Y.; Deng, L.; He, L.; et al. Wet/Sono-Chemical Synthesis of Enzymatic Two-Dimensional MnO<sub>2</sub> Nanosheets for Synergistic Catalysis-Enhanced Phototheranostics. *Adv. Mater.* **2019**, *31*, 1900401.s. [CrossRef]
31. Han, L.; Zhang, H.; Chen, D.; Li, F. Protein-directed metal oxide nanoflakes with tandem enzyme-like characteristics: Colorimetric glucose sensing based on one-pot enzymefree cascade catalysis. *Adv. Funct. Mater.* **2018**, *28*, 1800018. [CrossRef]
32. Prasad, P.; Gordijo, C.; Abbasi, A.; Maeda, A.; Angela, I.; Rauth, A.; DaCosta, R.S.; Wu, X.Y. Multifunctional albumin MnO<sub>2</sub> nanoparticles modulate aolid tumor microenvironment by attenuating hypoxia, acidosis, vascular endothelial growth factor and enhance radiation response. *ACS Nano* **2014**, *8*, 3202–3212. [CrossRef] [PubMed]
33. Liao, Q.Y.; Li, N.; Cui, H.; Wang, C.X. Vertically-Aligned Graphene@MnO Nanosheets as Binder-Free High-Performance Electrochemical Pseudocapacitor Electrodes. *J. Mater. Chem. A* **2013**, *1*, 13715–13720. [CrossRef]
34. Pachfule, P.; Shinde, D.; Majumder, M.; Xu, Q. Fabrication of carbon nanorods and graphene nanoribbons from a metal-organic framework. *Nat. Chem.* **2016**, *8*, 718–724. [CrossRef] [PubMed]
35. Xiao, Y.; Cao, M. Carbon-Anchored MnO Nanosheets as an Anode for High-Rate and Long-Life Lithium-Ion Batteries. *ACS Appl. Mater. Interfaces* **2015**, *7*, 12840–12849. [CrossRef] [PubMed]
36. Zhang, C.; Wang, J.; Jin, D.; Xie, K.; Wei, B. Facile fabrication of MnO/C core-shell nanowires as an advanced anode material for lithium-ion batteries. *Electrochim. Acta* **2015**, *180*, 990–997. [CrossRef]
37. Rekuć, A.; Bryjak, J.; Szymańska, K.; Jarzębski, A.B. Very stable silica-gel-bound laccase biocatalysts for the selective oxidation in continuous systems. *Bioresour. Technol.* **2010**, *101*, 2076–2083. [CrossRef]
38. Liu, Y.; Zeng, Z.; Zeng, G.; Tang, L.; Pang, Y.; Li, Z.; Liu, C.; Lei, X.; Wu, M.; Ren, P.; et al. Immobilization of laccase on magnetic bimodal mesoporous carbon and the application in the removal of phenolic compounds. *Bioresour. Technol.* **2012**, *115*, 21–26. [CrossRef]
39. Qiu, N.; Liu, Y.; Guo, R. Electrodeposition-assisted rapid preparation of Pt nanocluster/3D graphene hybrid nanozymes with outstanding multiple oxidase-like activity for distinguishing colorimetric determination of dihydroxybenzene isomers. *ACS Appl. Mater. Interfaces* **2020**, *12*, 15553–15561. [CrossRef]
40. Wang, X.; Liu, J.; Qu, R.; Wang, Z.; Huang, Q. The laccase-like reactivity of manganese oxide nanomaterials for pollutant conversion: Rate analysis and cyclic voltammetry. *Sci. Rep.* **2017**, *7*, 7756. [CrossRef]
41. Wu, H.; Xia, L.; Ren, J.; Zheng, Q.; Xu, C.; Lin, D. A high-efficiency N/P co-doped graphene/CNT@porous carbon hybrid matrix as a cathode host for high performance lithium-sulfur batteries. *J. Mater. Chem. A* **2017**, *5*, 20458–20472. [CrossRef]
42. Zhang, H.; Zhang, Y.; Bai, L.; Zhang, Y.; Sun, L. Effect of physiochemical properties in biomass derived materials caused by different synthesis methods and their electrochemical properties in supercapacitors. *J. Mater. Chem. A* **2021**, *9*, 12521–12552. [CrossRef]
43. Xing, L.; Chen, X.; Tan, Z.; Chi, M.; Xie, W.; Huang, J.; Liang, Y.; Zheng, M.; Hu, H.; Dong, H.; et al. Synthesis of porous carbon material with suitable graphitization strength for high electrochemical capacitors. *ACS Sustain. Chem. Eng.* **2019**, *7*, 6601–6610. [CrossRef]
44. Cai, R.; Yang, D.; Peng, S.; Chen, X.; Huang, Y.; Liu, Y.; Hou, W.; Yang, S.; Liu, Z.; Tan, W. Single nanoparticle to 3D supercage: Framing for an artificial enzyme system. *J. Am. Chem. Soc.* **2015**, *137*, 13957–13963. [CrossRef]
45. Chen, C.; Nan, C.; Wang, D.; Su, Q.; Duan, H.; Liu, X.; Zhang, L.; Chu, D.; Song, W.; Peng, Q.; et al. Mesoporous multicomponent nanocomposite colloidal spheres: Ideal high-temperature stable model catalysts. *Angew. Chem.* **2011**, *50*, 3725–3729. [CrossRef]
46. Lv, R.; Sun, S.; Liu, J.; Wang, K.; Golubev, Y.A.; Dong, F.; Kotova, O.B.; Kotova, E.L.; Nie, X.; Tan, D. Bifunctional nanozyme of copper organophyllosilicate for the ultrasensitive detection of hydroquinone. *Anal. Bioanal. Chem.* **2022**, *414*, 1039–1048. [CrossRef]
47. Zhao, X.; Lyu, H.; Yao, X.; Xu, C.; Liu, Q.; Liu, Z.; Zhang, X.; Zhang, X. Hydroquinone colorimetric sensing based on platinum deposited on CdS nanorods as peroxidase mimics. *Microchim. Acta* **2020**, *187*, 587. [CrossRef]
48. Wang, X.; Zhao, M.; Songa, Y.; Liu, Q.; Zhang, Y.; Zhuang, Y.; Chen, S. Synthesis of ZnFe<sub>2</sub>O<sub>4</sub>/ZnO heterostructures decorated three-dimensional graphene foam as peroxidase mimetics for colorimetric assay of hydroquinone. *Sens. Actuators B Chem.* **2019**, *283*, 130–137. [CrossRef]
49. Zheng, X.; Liu, Z.; Lian, Q.; Liu, H.; Chen, L.; Zhou, L.; Jiang, Y.; Gao, J. Preparation of flower-like NiMnO<sub>3</sub> as oxidase mimetics for colorimetric detection of hydroquinone. *ACS Sustain. Chem. Eng.* **2021**, *9*, 12766–12778. [CrossRef]
50. Song, Y.; Zhao, M.; Li, H.; Wang, X.; Cheng, Y.; Ding, L.; Fan, S.; Chen, S. Facile preparation of urchin-like NiCo<sub>2</sub>O<sub>4</sub> microspheres as oxidase mimetic for colorimetric assay of hydroquinone. *Sens. Actuators B Chem.* **2018**, *255*, 1927–1936. [CrossRef]
51. Tran, T.D.; Nguyen, P.T.; Le, T.N.; Kim, M. DNA-copper hybrid nanoflowers as efficient laccase mimics for colorimetric detection of phenolic compounds in paper microfluidic devices. *Biosens. Bioelectron.* **2021**, *182*, 113187. [CrossRef] [PubMed]
52. Dang, T.V.; Heo, N.S.; Cho, H.J.; Lee, S.M.; Song, M.Y.; Kim, H.J.; Kim, M. Colorimetric determination of phenolic compounds using peroxidase mimics based on biomolecule-free hybrid nanoflowers consisting of graphitic carbon nitride and copper. *Microchim. Acta* **2021**, *188*, 293. [CrossRef] [PubMed]
53. Liu, Y.; Wang, Y.; Zhu, W.; Zhang, C.; Tang, H.; Jiang, H. Conjugated polymer nanoparticles-based fluorescent biosensor for ultrasensitive detection of hydroquinone. *Anal. Chim. Acta* **2018**, *1012*, 60–65. [CrossRef] [PubMed]
54. Wu, X.; Gao, X.; Xu, L.; Huang, T.; Yu, J.; Wen, C.; Chen, Z.; Han, J. Mn<sub>2</sub>O<sub>3</sub> doping induced the improvement of catalytic performance for oxygen reduction of MnO. *Int. J. Hydrogen Energy* **2016**, *41*, 16087–16093. [CrossRef]

55. Arunchander, A.; Vivekanantha, M.; Peeraa, S.G.; Sahu, A.K. MnO–nitrogen doped graphene as a durable non-precious hybrid catalyst for the oxygen reduction reaction in anion exchange membrane fuel cells. *RSC Adv.* **2016**, *6*, 95590–95600. [[CrossRef](#)]
56. Chen, R.; Yan, J.; Liu, Y.; Li, J. Three-dimensional nitrogen-Doped graphene/MnO nanoparticle hybrids as a high-performance catalyst for oxygen reduction reaction. *J. Phys. Chem. C* **2015**, *119*, 8032–8037. [[CrossRef](#)]
57. Wu, Q.; Jiang, M.; Zhang, X.; Cai, J.; Lin, S. A novel octahedral MnO/RGO composite prepared by thermal decomposition as a noble-metal free electrocatalyst for ORR. *Mater Sci.* **2017**, *52*, 6656–6669. [[CrossRef](#)]
58. Ding, J.; Ji, S.; Wang, H.; Brett, D.J.L.; Pollet, B.J.; Wang, B.G. MnO/N-doped mesoporous carbon as advanced oxygen reduction reaction electrocatalyst for zinc-air batteries. *Chem. Eur. J.* **2019**, *25*, 2868–2876. [[CrossRef](#)]
59. Luo, W.; Chou, S.; Wang, J.; Zhai, Y.; Liu, H. A facile approach to synthesize stable CNTs@MnO electrocatalyst for high energy lithium oxygen batteries. *Sci. Rep.* **2015**, *5*, 8012. [[CrossRef](#)]
60. Edmund, C.M.T.; David, S.; Danielle, L.G.; Thomas, B.R.; Andrew, A.G. Multicopper models for the laccase active site: Effect of nuclearity on electrocatalytic oxygen reduction. *Inorg. Chem.* **2014**, *53*, 8505–8516.
61. Roche, I.; Chaînet, E.; Chatenet, M.; Vondrák, J. Carbon-supported manganese oxide nanoparticles as electrocatalysts for the oxygen reduction reaction (ORR) in alkaline medium: Physical characterizations and ORR mechanism. *J. Phys. Chem. C* **2007**, *111*, 1434–1443. [[CrossRef](#)]